Nanoarchitectonics towards Full Coverage of CdZnS Nanospheres by Layered Double Hydroxides for Enhanced Visible-light-driven H_2 Evolution

Yang Ming[a,b], Zhixing Cheng[a], Shuo Shi[a], Jing Su[c], Weng-Fu Io[d], Hanbai Wu[e], Jiashen Li[f], Fen Pan[g], Bin Fei[a,b,*]

(a) School of Fashion & Textiles, The Hong Kong Polytechnic University, Hong Kong, P.R. China

(b) Research Centre for Resources Engineering towards Carbon Neutrality, The Hong Kong Polytechnic University, Hong Kong, P.R. China

(c) College of Textile Science and Engineering, Jiangnan University, Jiangsu, P.R. China

(d) Department of Applied Physics, The Hong Kong Polytechnic University, Hong Kong, P.R. China

(e) Department of Biomedical Engineering, City University of Hong Kong, Hong Kong, P.R. China

(f) Department of Materials, University of Manchester, United Kingdom

(g) School of Advanced Materials, Peking University Shenzhen Graduate School, Shenzhen, P.R. China.

* Corresponding author, E-mail: bin.fei@polyu.edu.hk

Abstract

Nanoarchitectonics of semiconductors shed light on efficient photocatalytic hydrogen evolution (PHE), by precisely controlling the surface microenvironment of cocatalysts. Taking cadmium zinc sulfide (CZS) nanoparticles as targets, the spontaneous modifications were conducted by interactions between surface Cd^{2+}/Zn^{2+} atoms and thiol groups in thioglycolic acid. The capping ligand impacts the semiconductor surface with a negative electronic environment, contributing to the full coverage of CZS by nickel-cobalt hydroxides (NiCo-LDHs). The obtained core-shell CZS@NiCo-LDHs, possessing a shell thickness of ~ 20 nm, exhibits a distinguished topology (S_{BET}= 87.65m^2/g), long surface carrier lifetime, and efficient charge-hole separation. Further photocatalytic hydrogen evaluation demonstrates an enhanced H_2 evolution rate of 18.75 mmol g^{-1} h^{-1} with an apparent quantum efficiency of 16.3% at 420 nm. The recorded catalytic performance of core-shell sample is 44.6 times higher than that of pure CZS nanospheres under visible light irradiation. Density functional theory simulations indicate that sulfur atoms play the role of charge acceptor and surface Ni/Co atoms are electron donors, as well as a built-in electric field effect in the direct Z-scheme can be established. Altogether, this work takes advantages of strong S affinity from surface metal atoms, revealing the interfacial engineering, towards improved visible light driven PHE activity.

Keywords: Photocatalytic hydrogen evolution, CZS@NiCo-LDHs, core-shell structure, Direct Z-scheme, built-in electric field.

1. Introduction

Utilization of solar energy towards the production of hydrogen and oxygen is a promising way to realize a carbon-neutral society[1–4]. Hence, efficient visible-light-induced photocatalytic hydrogen evolution (PHE) is currently attractive. This reaction requires suitable cocatalysts that possess high light absorption capability, abundant exposed catalytic active sites, and efficient charge transfer capability. Cadmium zinc sulfide (CZS), as a typical semiconductor with a narrow band gap (2.5 eV), shows promising potential towards visible-light-driven PHE[5,6]. However, the serve photocorrosion, and fast electron-hole recombination impede CZS's practical application, which is in urgent demands of cocatalyst loading. Under this condition, the morphology and distribution of cocatalysts on semiconductors significantly impact the final catalytic performance. The core-shell structure, as a result, attracts increased attention due to the large specific surface areas, abundant active sites, and shortened carrier diffusion pathways. Chen *et al.*[7] successfully instructed the integration of CuS cocatalyst by carefully injecting Cu-S seeds into a cationic (Cd/Zn) precursor solution, followed by the solvothermal reaction. The selective decoration of CuS onto CZS nanorods is ultimately realized by controlling all experimental factors, including temperature, feeding speed and ratios between copper and CZS. More recently, Ma *et al.*[8] reported the incorporation of NiS nanoparticles into the CZS system, by one-pot hydrothermal synthesis. The distribution of cocatalysts, however, is highly dependent on the mixture status during the synthetic process, as the trapped NiS particles inside composites are rarely exposed to water molecules. Herein, surface modifications of the CZS surface at mild conditions are successfully conducted by adopting a capping agent with strong metal affinity. This engineering contributes to the full coverage of CZS by nickel-cobalt layered double hydroxides, with distinguished interface, and abundant active sites.

As indicated, most cocatalysts decorated onto semiconductor systems are fabricated by the one-pot method[9–11]. While disorderly introducing transition metal atoms may distort the heterostructure, further limiting the PHE activity. Nanoarchitectonics[12,13], as a result, sheds light on the construction of electron tunnel for improving electron-hole separation in semiconductor and charge transfer from CZS to cocatalysts. Obviously, the poor interfacial interaction between the semiconductor and cocatalyst acts like a "wall", hindering the efficient transportation of charge flow. Therefore, the core-shell structure is more expected to be a promising solution, by growing the shell layer as electron acceptors and active sites. After investigating the ligand-nanoparticles interactions, researches have been reported that the ligand capping agent (e.g. oleyl amine[14], dichlorodiphenyltrichloroethane[15]) on CZS quantum dots can significantly influence products' morphologies and band structures. The surface capping agent is further confirmed to have little impacts when particle size is larger than several nanometers, since the crystal domain has been

formed and already stabilized the whole semiconductor system. However, it is believed that the capping agent although has little effects on band structure, does change the semiconductor's surface micro-environment, where one can manifest this situation for constructing heterostructure. Moreover, transition metal-based catalysts such as metal dichalcogenide[16], and metal oxides[17], have been intensively investigated for water splitting reactions. Recently, metal hydroxides have been attracting interest, due to their easy fabrication in moderate situation and potential in large-scale industrial applications. However, no such study has been reported to construct a true core-shell structure between semiconductors and hydroxides.

This study presents a facile synthetic method to prepare a core-shell CZS@NiCo layered double hydroxide (NiCo-LDHs) cocatalyst with a distinguished interfacial structure. The synthesis process involves surface modification of CZS with thioglycolic acid (TGA), followed by in-situ dethiolation and hydrothermal loading of the electrocatalyst. The successful surface modification is firstly confirmed by simulation. Further experimental zeta potential (-5.96 mV) of modified CZS surface facilitates strong ionic interaction between M^{2+} ions and carboxyl groups (in TGA site). Consequently, a CZS@NiCo-LDHs cocatalyst with an average diameter of 130 nm and a firm LDH shell thickness of ~20 nm is obtained. The close contact core-shell structure possesses a hierarchical topology (S_{BET}= 87.69 m^2/g), allowing for easy diffusion of electrolytes, rapid electron-hole separation, and efficient transfer of photogenerated electrons. The NiCo-LDHs act as active water-splitting electrocatalysts, receiving separated electrons from CZS. The high coverage of LDHs on CZS results in a high PHE rate of ~18.75 mmol g^{-1} h^{-1}, with favorable photostability in 5 cycles under visible light irradiation. Density function theory calculations show an apparent redistribution of electron density after introducing LDHs, and density of states (DOS) of the heterostructure possess an improved electron conductivity at Fermi level, facilitating the electron transfer, and charge separation. This work opens a new avenue by adopting a capping agent to change the surface electronic environment, which is further employed for the construction of heterostructure.

2. Results and Discussions

2.1 Conceptual Design and Nanoarchitectonics on CZS Nanospheres

As indicated in scheme 1, the CZS nanospheres with exposed Cd/Zn atoms at the surface are synthesized by a solvothermal method. The surface modification of CZS was conducted in an alkaline medium at ambient conditions, which is supposed to provide a negatively charged surface. The electrostatic interaction, as a result, drives the sorption of metal cations and facilitates the full coverage of CZS by LDHs during the hydrothermal process.

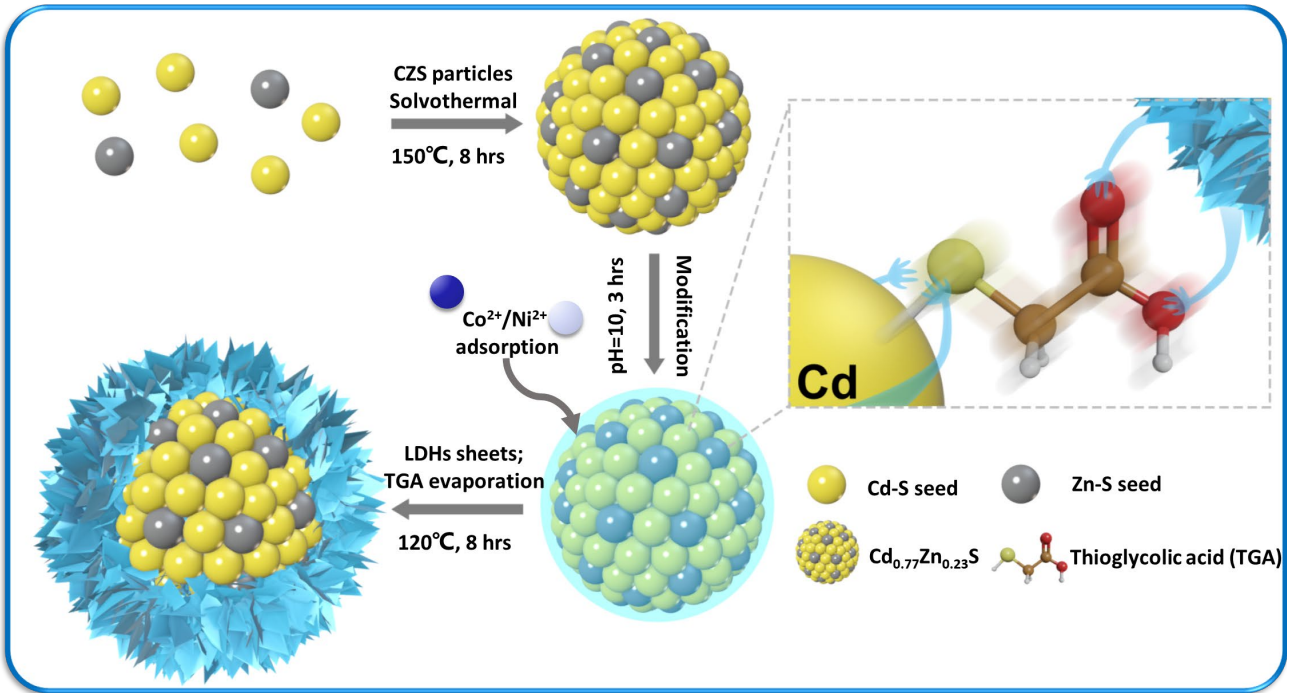

Scheme 1. Illustration of the synthetic process for CZS@NiCo-LDHs core-shell photocatalyst.

To verify the advantage of this conceptual design, the feasibility of small molecule modification and construction of CZS/NiCo-LDHs heterostructure were firstly examined by density function simulations. The optimized thioglycolic acid molecules on CZS surface suggest the bond length of Cd-S and Zn-S are 2.57 Å and 2.49 Å (**Fig.1 a**), close to the crystal Cd-S (2.55 Å) and Zn-S bond length (2.41 Å). Subsequently, the adsorption energies of one TGA molecule onto CZS surface (**Table S2, Fig.1 b**) were calculated. The adsorption energies of acid molecules on top of Cd and Zn atoms are -2.03 eV and -1.08 eV, respectively, suggesting a favorably spontaneous adsorption on CZS (101) surface. Besides, the molecule tends to be adsorbed onto Cd atom firstly, followed by Zn atom. By constructing CZS/NiCo-LDHs heterointerface (**Fig.S1**), the resultant charge density difference plot (**Fig.1 c, S2**) along heterostructure indicates an electron redistribution, which originates from the contact potential difference between CZS and LDHs. In this heterostructure, S atoms are the electron-rich region, and Co/Ni atoms are the electron depletion region. Such electron redistribution at interface induces a built-in electric field, which has been reported to facilitate the water molecule adsorption and dissociation process[18]. Moreover, DOS plots were calculated to investigate the electron accumulation level in pristine semiconductors and heterostructure. As indicated in **Fig.1 d**, CZS semiconductor and NiCo-LDHs possess a band gap of 2.48 eV and 2.04 eV, close to the measured UV-vis spectrum results. Typically, the calculated band gap based on the generalized gradient approximation (GGA) exchange correlation function will be smaller than the practical value, due to the underestimation by the GGA function[19]. Meanwhile, a further increase in the electron density at the Fermi level after introducing one-layer of LDHs can be observed,

suggesting an improved electron conductivity. Such improvement is supposed to contribute to better electron transportation at the interface, leading to an enhanced catalytic performance. Therefore, it is believed that constructing a strongly coupled interface between CZS and NiCo-LDHs via surface modification can boost photocatalytic hydrogen evolution.

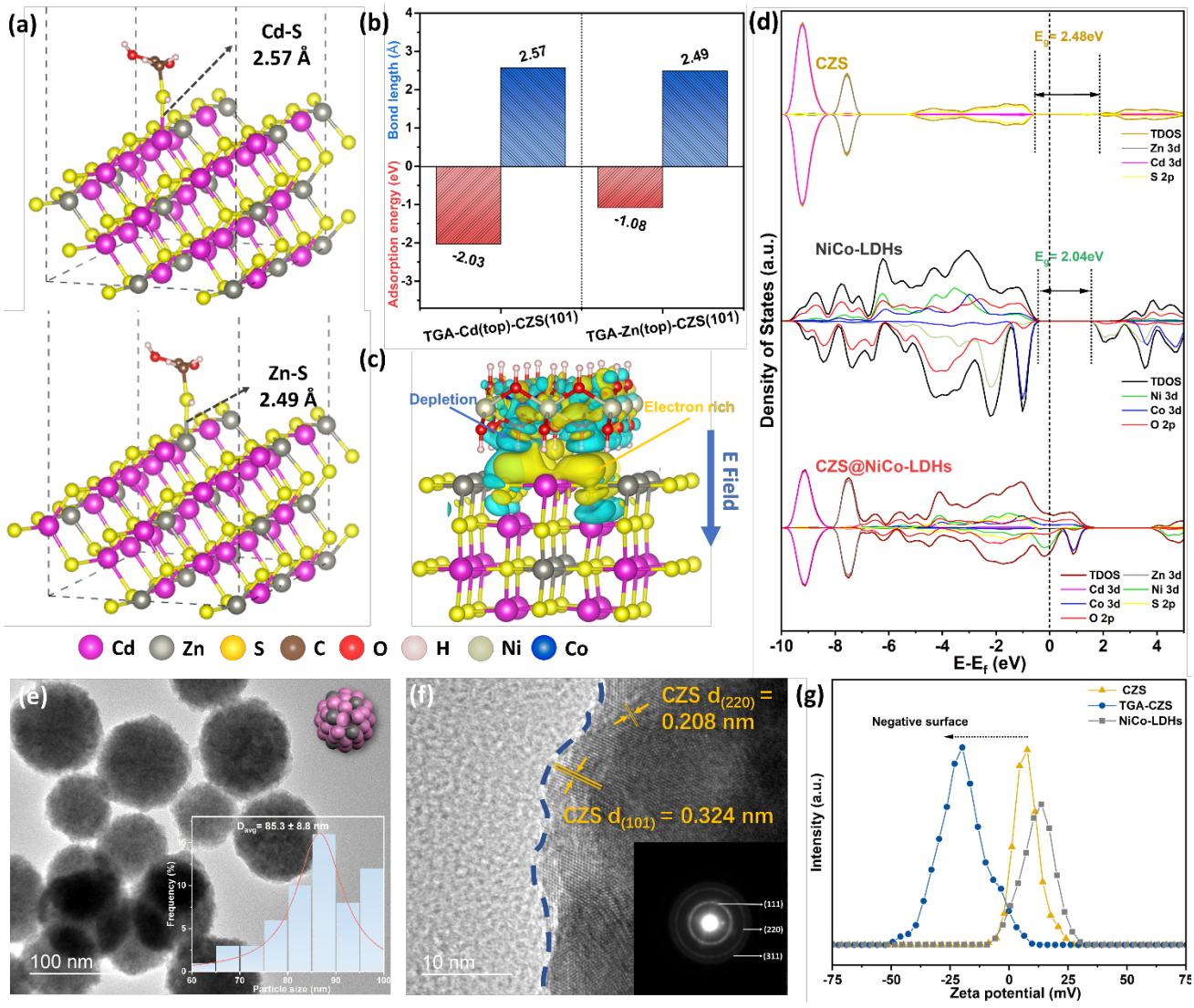

Figure.1 (a) Optimized geometry of one thioglycolic acid (TGA) molecule on the CZS (101) plane (upper: on top site of Cd atom, lower: on top site of Zn atom); (b) Summary of bond length and adsorption energy of TGA molecule on top of Cd and Zn atoms; (c) Charge density different plot of CZS-NiCo-LDHs heterostructure; (d) Density of state (DOS) plots of CZS, NiCo-LDHs and heterostructure; (e) Transmission electron microscopy (TEM) and (f) High-resolution TEM (HRTEM) of cadmium zinc sulfide (CZS) nanospheres (insert: particle size distribution and selected area electron diffraction pattern); (g) ζ-potential plots of CZS, Thioglycolic acid modified CZS (TGA-CZS) and NiCo-layered double hydroxides in aqueous solution (pH~ 7).

Subsequently, the cadmium zinc sulfide nanospheres, possessing an average diameter of 85.3±8.8 nm

(**Fig.1 e, S3 a**), are synthesized and selected as targets. The selected area electron diffraction ring refers to the polycrystalline structure of CZS, attributing to the bulk lattice fringe of CZS (111), (220), and (311), respectively[20]. High-resolution TEM (**Fig.1 f**) at the CZS surface edge indicates the lattice planes of 0.208 nm and 0.324 nm, which are assigned to the (220) and (101) planes [20], respectively. From HRTEM results, it is assumed that the surface layer of CZS is covered by Cd and Zn atoms from the (101) plane, which is also employed in DFT simulations. It is further noticed the as-synthesized spheres possess a pomegranate-liker morphology. This phenomenon can be related to the fact that Cd/Zn-S seeds are supposed to aggregate first, then form nanocluster as the seed center, where more Cd and Zn-S bonds attach onto the cluster center forming larger nanosphere. Inductively coupled plasma-optical emission spectrometry (ICP-OES) was then employed to reveal the stoichiometric ratio between Cd and Zn, which is determined to be $C_{0.768}Z_{0.232}S$ (**Table S1**) and is similar to the input ratio. In order to calculate the molar amount of employed thioglycolic acid in surface modification, we conducted calculations by identifying inorganic part and surface Cd/Zn atoms ratio based on several assumptions [15] (**Fig.S4**). Additionally, ζ-potential technique was conducted to explore the surface electronic environment of CZS before and after modification. As illustrated in **Fig.1 g**, the measured ζ-potential in aqueous dispersion of TGA-CZS shift more negative from 7.96 mV to -24.58 mV, leading to a stronger cation ion attraction ability. This positive effect contributes to the subsequent growth of LDHs, consistent with simulation results that the carboxyl group provides a more negative electronic environment. The pure NiCo-LDHs in ethanol dispersion possess a zeta potential of 13.86 mV, showing that NiCo-LDHs have little chance of being physically adsorbed on the CZS surface without surface modification. Meanwhile, the morphology of CZS after thioglycolic acid modification were examined by TEM with little distortion (**Fig.S3 b-c**).

2.2 Morphological and Physical Characterization of Cocatalysts

The NiCo-LDHs cocatalysts, as depicted in **Fig.2a, S5a**, exhibit a nanoflower morphology after hydrothermal treatment[21]. Thereby, this structure demonstrates a capability for complete coverage of the CZS nanosphere surface. Meanwhile, ICP-OES results suggest the stoichiometric ratio of LDHs is $Ni_{0.752}Co_{0.248}$-LDHs (**Table S1**), which is close to the designed ratio. As a result of successful surface modification, TEM images and high-angle annular dark-field scanning TEM (HADDF-STEM) of CZS@NiCo-LDHs illustrate the well-constructed core-shell structure (**Fig.2 b, e and Fig.S5 b**), with an average shell thickness of ~24 nm. (**Fig.2 c**). Further high-resolution TEM images (HRTEM, **Fig.2 d, Fig.S6**) confirm the interfaces between CZS nanospheres and NiCo-LDHs. The lattice fringes of 0.208 nm and 0.175 nm are attributed to the (220) facet of CZS nanospheres and the (001) facet of NiCo-LDHs, respectively[19]. Besides morphologies, EDS elemental mappings (**Fig.2 f-k**) were recorded to show the distribution of elements. As illustrated, the core of nano-flower

is composed of CZS semiconductor, meanwhile, the shell from EDS mapping is consisting of Ni and Co elements with a thickness of ~20 nm, in good coordination with HRTEM image. Such well-defined structure is also observed in CZS@Ni-LDHs sample but possesses thinner shell thickness (**Fig.S5 c-d**). However, the CZS/NiCo-LDHs composites (**Fig.S7 a-d**) exhibits random structure of a mixture of CZS semiconductor and LDHs. Such a mixture causes a loose interfacial interaction between semiconductors and catalysts, which may further lead to poor electron transfer during PHE.

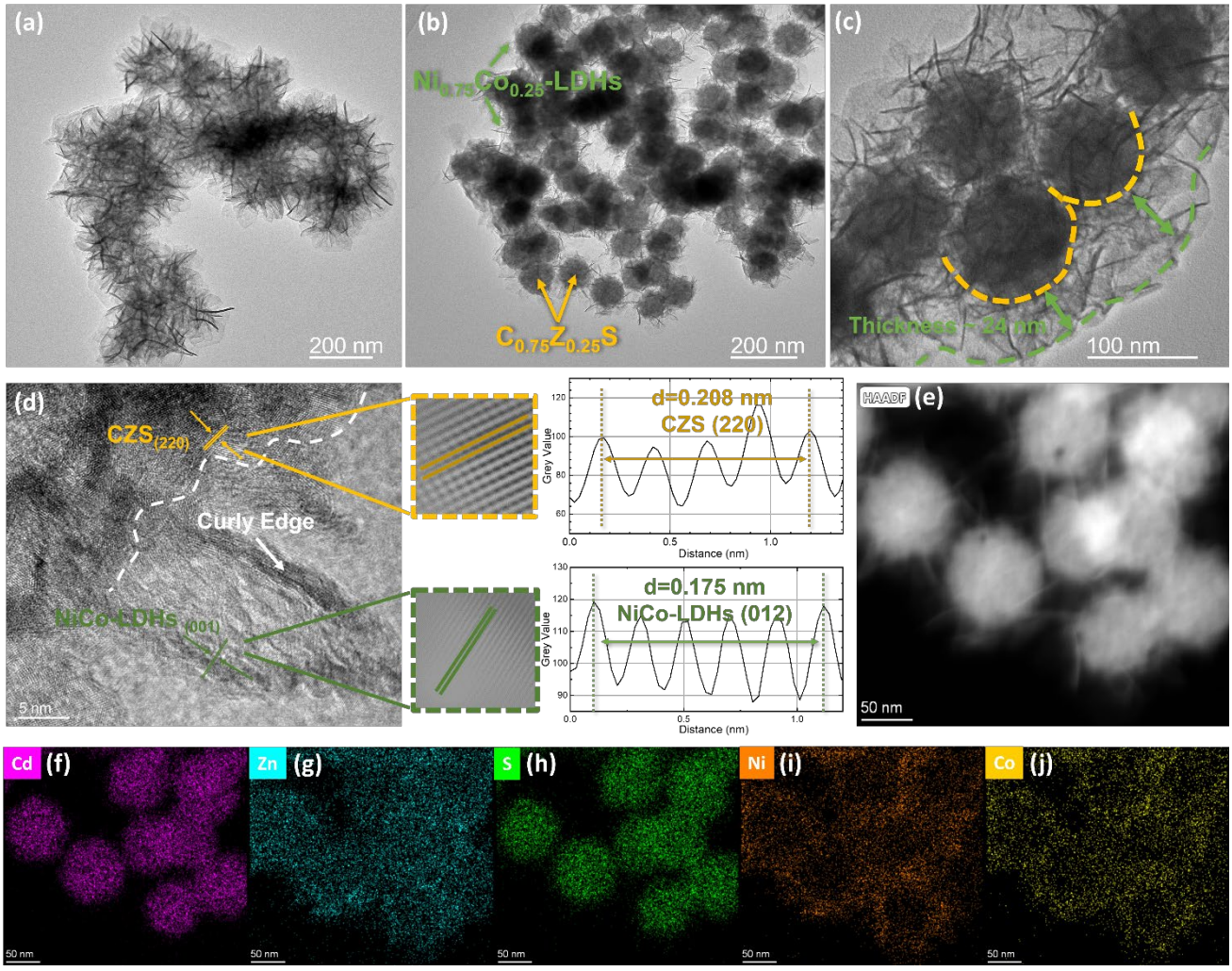

Figure 2. TEM images of (a) NiCo-LDHs, CZS@NiCo-LDHs core-shell structure at (b) low and (c) high magnification; (d) HRTEM image of selected area (enlarged figure: inverse fast Fourier transform (FFT) image of corresponding CZS and NiCo-LDHs lattice spacing); (e) High-angle annular dark-field imaging- scanning transmission electron microscopy (HADDF-STEM) image; and (f-j) Corresponding energy dispersive spectroscopy (EDS) for elemental mapping of Cd, Zn, S, Ni, Co.

XRD patterns (**Fig.3 a**) were recorded to investigate the crystal structures of each component. The XRD pattern of CZS shows a typical sphalerite diffraction pattern, where characteristic peaks of

26.5°, 43.9° and 52.2° are attributed to the cadmium zinc blende (111), (220), (311) lattice plane[19,22](greenockite CdS JPCDS: 41-1409; sphalerite ZnS JPCDS: 05-0566). After introducing Ni hydroxides and NiCo-LDHs into the CZS system, new peaks representing β-$Ni(OH)_2$ (JPCDS: 14-0117) are observed at 19.1°, 32.9°, 39.4°, 51.8°, 58.8°, and 63.5°, correspondingly[23,24]. Notably, the incorporation of cobalt ions into Ni LDHs (NiCo-LDHs) results in a negative shift towards a lower degree (~0.4°). This shift can be attributed to the introduction of cobalt ions leading to a larger lattice space. Moreover, two additional peaks at 34.3° and 38.5° are determined as β-$Co(OH)_2$ phase (JCPDS: 74-1057)[25]. The XRD pattern of the CZS@NiCo-LDHs sample exhibits a significant decrease in the intensity of β-$Ni(OH)_2$ peaks, which can be owing to the strongly coupled interfaces. More specifically, the LDHs in CZS@NiCo-LDHs are predominantly adhered to the surface of CZS core in forms of thin layer, rather than being as separate entities in the composite sample (CZS/NiCo-LDHs). Raman spectrum (**Fig.S8**) was then conducted to double confirm the chemical bonds in samples. The peaks identified at 321.6 cm^{-1} and 623.1 cm^{-1} are recognized as 1st and 2nd plasmon-optical phono modes of CZS[26]. While peaks located at 529.8 cm^{-1} are recognized as Ni-OH bonds in Ni hydroxides[27,28], which are consistent with results from XRD pattern.

The N_2 adsorption and desorption isotherm (**Fig.S9**), followed by pore size distribution (**Fig.3 b**) analysis were employed to investigate the topography of various photocatalysts. The NiCo-LDHs synthesized in this work possessed a high BET surface area (S_{BET} = 207.38 m^2/g), originating from the macroscopical flower-like structure and periodic interlamellar space at the microscale[29]. The core-shell sample (CZS@NiCo-LDHs) benefits from the high surface area of LDHs and a well-defined interface, which result in the highest surface area (S_{BET} = 87.69 m^2/g), compared to that of CZS@Ni-LDHs (S_{BET} = 28.5 m^2/g) and CZS/NiCo-LDHs (S_{BET} = 45.69 m^2/g). The property of high surface area, as a result, can facilitate the electrolyte diffusion in the core-shell sample. Notably, the original CZS nanosphere has a surface area of 30.89 m^2/g, likely due to the aggregation of Cd/Zn-S seed during synthesis and finally leads to the formation of micropores within the semiconductor. Moreover, a clear hierarchical topology in pore size distribution is identified in CZS@NiCo-LDHs, where both micropores (r ~ 0.5 nm) and mesopores (r ~ 1.2nm) exist. Moreover, we also conducted the water contact angle analysis (**Fig.3 c**) by dispersing the powders onto the FTO glass. The original glass possesses a relative more hydrophobic surface (θ = 106.46°) compared with that of CZS powder covered surface (45.87°). After loading CZS@NiCo-LDHs and pristine NiCo-LDHs, the contact angles further decrease to 40.32° and 41.51°, proving the hydrophilic structure of the core-shell sample.

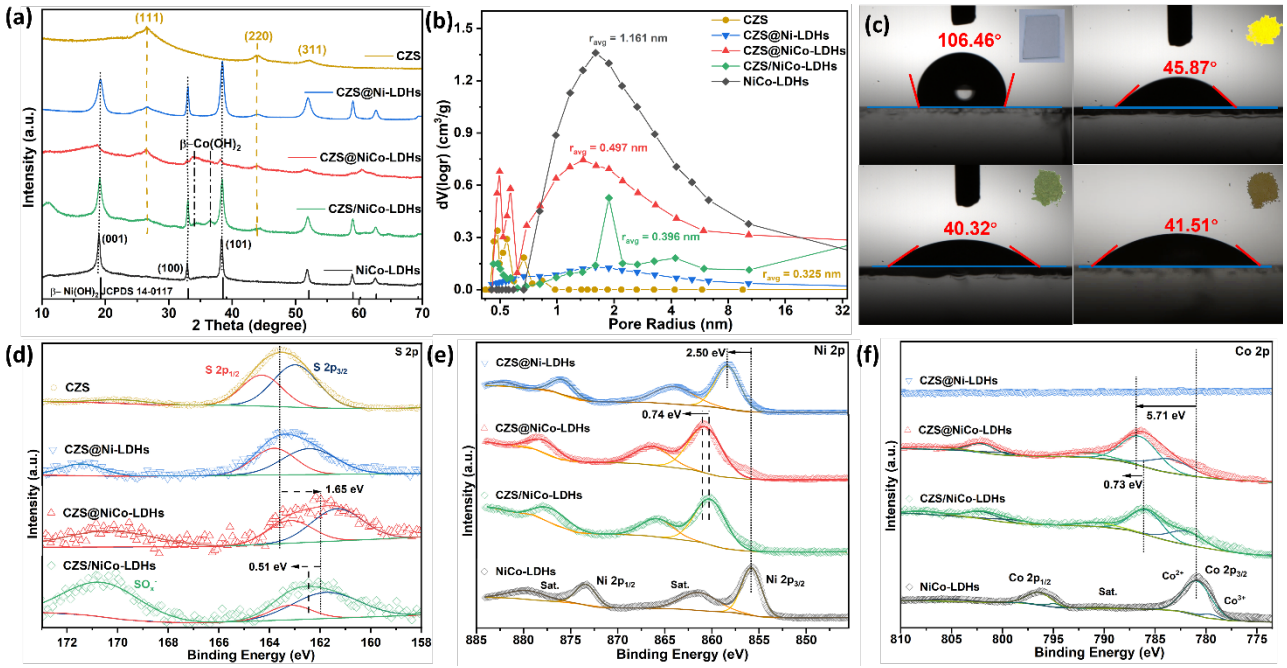

Figure 3. (a) X-ray diffraction patterns, (b) Pore size distributions of CZS, CZS@NiCo-LDHs, NiCo-LDHs, CZS/NiCo-LDHs, and NiCo-LDHs; (c) Water contact angles of FTO glass substrate, CZS, CZS@NiCo-LDHs, NiCo-LDHs, CZS/NiCo-LDHs, and NiCo-LDHs; X-ray photoelectron spectroscopy of (d) S 2p, (e) Ni 2p, (f) Co 2p of corresponding samples.

XPS analysis (**Fig.S10**) was conducted to investigate the surface chemical states, composition, proves the changes in Ni and cobalt electronic environment. It should be noted that the XPS spectrum of Cd 3d (Fig.S11 a) possesses a significant positive shift (~5.91 eV) for both core-shell (CZS@NiCo-LDHs) and composite samples (CZS/NiCo-LDHs), indicating a strong interfacial interaction. However, it is interesting that the signal of Zn 2p (**Fig.S11 b**) for CZS@ Ni-LDHs and NiCo-LDHs decrease, compared with that of pristine CZS and composites. This weakening effect may be attributed to the fact that XPS is a surface sensitive technique with a resolution ~10nm. Meanwhile in the core-shell sample, the shell of LDHs is up to 20 nm. In addition, a slight shift (~0.5 eV) towards higher binding energy is noticed, suggesting a weak interaction of Zn atom, compared to surface atoms. Furthermore, the negative shift (1.65 eV) of S 2p spectrum (**Fig.3 d**) towards lower binding energy is observed[30,31]. With respect to the Ni and Co 2p spectrum, the deconvoluted peaks are assigned to the electron spin doublet and satellite. Specifically, peaks in NiCo-LDHs (**Fig.3 e-f**) located at 780.91 eV and 796.18 eV are attributed to Co $2p_{3/2}$ and $2p_{1/2}$, respectively[24,32]. The peaks observed at 855.89 eV and 873.37 eV are assigned to Ni $2p_{3/2}$ and $2p_{1/2}$, accordingly[33]. Additionally, Co^{3+} valence state (779.54 eV) is identified in Co 2p spectrum of pure NiCo-LDHs, while a shift towards higher binding energy is observed in core-shell (5.71 eV) and composite samples (4.98 eV). It should be noticed that Co^{2+} state is more stable than Co^{3+}, which requires more energy to excite the core-level electrons in Co^{3+} orbital. The ration between Co^{3+} and Co^{2+} in CZS@NiCo-LDHs is 0.53

and 0.59 for CZS/NiCo-LDHs, with similar oxidized Co^{2+} ions into LDHs frameworks. The corresponding movement in Co, Ni and S 2p spectrum indicates a strong interfacial interaction, compared with that of composites. Meanwhile, it can be deducted that the S atoms are the electron acceptor, due to the high electron affinity.

2.3 Photo/electrocatalytic Performance

The photocatalytic hydrogen evolution measurements of all samples were conducted under visible light region (λ>420 nm) using 10 v% TEOA aqueous solution as hole sacrificial agent and Eosin Y as dye sensitization system for pure NiCo-LDHs. As illustrated in **Fig.4 a**, the original CZS semiconductor exhibits low photocatalytic activity (1.31 mmol g^{-1} over 4 hrs), even though the adsorption region of the CZS semiconductor lies under the visible region. The low activity can be attributed to the limited catalytic sites on the CZS surface. It has been reported that the most possible active sites are Zn vacancies-V_{Zn} [34]. Due to the dye sensitization system as visible light absorber[35], NiCo-LDHs shows surprisingly high PHE activity, which is beyond 10 mmol g^{-1} in 4 hrs irradiation. Nevertheless, H_2 accumulated evolution test of CZS@Ni-LDHs, CZS @NiCo-LDHs, and CZS/NiCo-LDHs compounds are 27.42 mmol g^{-1}, 69.72 mmol g^{-1} and 28. 47 mmol g^{-1}, respectively. The PHE rate of each sample normalized to mass was summarized in **Fig.4 b**, which clearly shows the activity enhancement of core-shell samples. The PHE rate of CZS@NiCo-LDHs reaches to 18.75 mmol g^{-1} h^{-1}. Such outstanding catalytic performance is around 44 times better than pristine CZS system (0.42 mmol g^{-1} h^{-1}), ~3 times higher than that of pure NiCo-LDHs (7.94 mmol h^{-1} g^{-1}). We also investigated the performance of $Ni(OH)_2$@CZS and NiCo-DLHs/CZS composites. The CZS/NiCo-LDHs shows a moderate PHE activity of 8.75 mmol h^{-1} g^{-1}, indicating that the electron-hole separation is insufficient. Moreover, the stability test of CZS@NiCo-LDHs shows a slight decrease in the accumulated amount of H_2 to 61.50 mmol h^{-1} g^{-1} (**Fig.4 c**, ~12.2%), indicating the sluggish photocorrosion effect (~50% catalytic degradation in CZS/NiCo-LDHs). This enhancement in the stability test suggests a superior electron transfer capability and abundant in active sites, which mitigate the electron-hole combination in CZS@NiCo-LDHs. We also differentiated the feed ration by gradually increasing the amount of Ni/Co precursor solution (**Fig.S12, S13**). The optimized 15v% of precursor solution shows the optimized evolution rate, while excessive amount of LDHs hinders the photocatalytic performance. To verify the internal efficiency of the core-shell sample, we measured the apparent quantum efficiency (AQE) by using various monochromatic filters (420 nm, 450 nm, 475 nm and 500 nm). The AQE of CZS@NiCo-LDHs at 420 nm reaches a value of 16.3%, and further decreases to 2.2% at 500 nm. These values outperform those of states-of-art CdS based photocatalysts in the literature (**Table S4**).

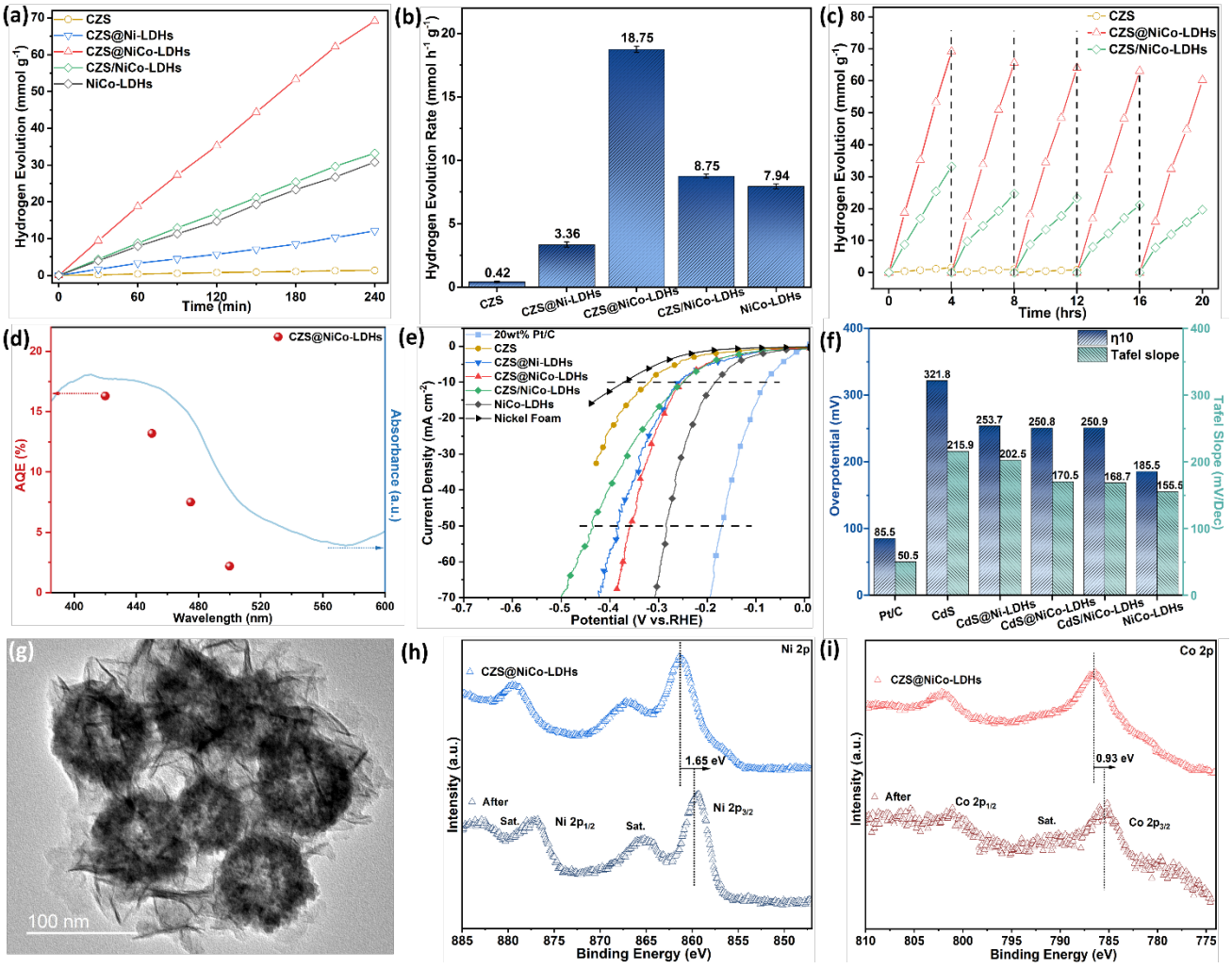

Figure 4. (a) Time course of photocatalytic H_2 evolution (PHE) and (b) PHE rate of CZS, CZS@Ni-LDHs, CZS@NiCo-LDHs, CZS/NiCo-LDHs, and NiCo-LDHs in 10 v% TEOA aqueous solution (amount of catalysts= 2.5 mg; note: Eosin Y, which functions as light absorption agent, is employed for pure NiCo-LDHs); (c) PHE stability test of CZS, CZS@NiCo-LDHs, and CZS/NiCo-LDHs over 20 hrs; (d) linear sweep voltammetry (LSV, scan rate = 5 mV/s), (e) Tafel slope and (f) column summary at different overpotentials, Tafel slope of commercial 20wt% Pt/C, CZS, CZS@Ni-LDHs, CZS@NiCo-LDHs, CZS/NiCo-LDHs, and NiCo-LDHs in 1_M KOH. (g) TEM, (h) Ni 2p and (i) Co 2p spectra before and after PHE stability test.

Further electrochemical measurement (**Fig.4 e-f**) and analysis were conducted in typical three-electrode system. Not surprisingly, NiCo-LDHs as typical electrocatalysts requires lowest overpotential of 185.5 mV and 313.8 mV to reach 10 mA cm^{-2} and 50 mA cm^{-2}, respectively. Moreover, the low Tafel slope suggests the NiCo-LDHs possesses a faster proton adsorption, hydrogen desorption kinetics, compared with those samples coupled with semiconductor. Compared with pristine $Ni(OH)_2$ and $Co(OH)_2$, the heteroatom doping into hydroxides can significantly lowered

the overpotential for HER[36]. Specifically, reports[23,29,37] have proven that the incorporation of Ni atoms in to β-$Co(OH)_2$ mitigates the adsorption energy of proton (ΔG_{H^*}) on the LDHs surface, which in turn facilitates the desorption of hydrogen gases. However, it is noticed that compared with catalytic performance of commercial Pt/C, the NiCo-LDHs may experience post treatment to exhibit enhanced catalytic performance. Post TEM and XPS (**Fig.4 g-i** and **S14**) analysis were conducted to examine the morphology distortion and electronic environment of samples after PHE cycle test. As indicated, the morphology of CZS@NiCo-LDHs maintains after 5 PHE cycles, with LDH shell and CZS nanospheres. It is further noticed that the photocorrosion still takes place at the center of CZS core, leading to a hollow structure. This hollow structure has been reported to be the electron deficiency induced corrosion, due to the lack of efficiency in electron-hole separation of pristine CZS spheres. In comparison, the nanocomposite sample exhibits a morphological distortion (**Fig.S15**) and separation between LDHs and CZS, indicating that the insufficient charge-hole separation causes the loss of catalytic efficacy. From XPS results, the Ni and Co 2p spectra shows little shift towards to lower binding energy slightly (1.65 eV and 0.93 eV, respectively). The Cd $3d_{5/2}$ and Zn $2p_{3/2}$ spectra (**Fig.S14**) shift back to 407.08 eV and 1022.eV, respectively, suggesting the decrease in LDHs' thickness with improved XPS signal at CZS surface. Interestingly, the signals in S 2p spectrum of core-shell sample are rarely detected. This absence of S element, as reported[38,39], originates from the photooxidative dissolution of CZS particles by adopting the following equation (1):

$$CdZnS(s) + 2O_2 \xrightarrow{h\upsilon} Cd/Zn(aq)^{2+} + SO_4(aq)^{2-} \quad (1)$$

2.4 Optical and Electrochemical Study

The steady state photoluminescence spectrum (**Fig.5 a**) was measured to investigate the photogenerated electron-hole pairs in CZS semiconductor, core-shell and composite samples. The intensity of luminescence peaks is directly related to the carrier recombination capability. As indicated in excitation spectrum of CZS, we employed wavelength of 340 nm as incident light source, and all emission peaks were centered at ~ 430 nm. The original semiconductor possesses highest intensity of PL emission peak, followed by CZS/NiCo-LDHs and CZS@NiCo-LDHs. This decreasing trend indicates that most electrons and holes in CZS recombine[6], instead of separation. For core-shell samples, most photoinduced electrons are possibly transferred to LDHs, as well as the complete coverage of CZS by LDHs passive electron-hole recombination. Moreover, it is noticed that the PL peak of CZS@NiCo-LDHs exhibits triplet emission peaks at 418, 441 and 471 nm, accordingly. These emission peaks, originating from the emission peaks of trap states, defects level of S and Zn[40],[6,36], may arise from the post hydrothermal treatment[41]. Further time-resolved PL spectrum (**Fig.5 b**) was conducted to evaluate the lifetime of electrons in samples. The corresponding biexponential fitting illustrates the composition of each electron with acceptable χ^2(shown in the

Table S3). The extend τ_1 and τ_2 electron is related to the intrinsic properties of excited electrons/carriers. The τ_2 of CZS@NiCo-LDHs (3.807ns with a portion of 37.26%) and CZS/NiCo-LDHs (0.901ns with a portion of 49.46%) is significantly shorter than that of pristine CZS (4.049 ns with a portion of 82.55%), indicating a low fluorescence decay time of carries and a possible transfer to cocatalysts. Meanwhile, τ_3 of core-shell samples (19.683 ns) exhibit an obvious increase compared with that of composite samples (4.721 ns). This phenomenon suggests a sufficient electron-hole separation on the surface of the core-shell sample[42], owing to the full coverage of LDHs and strongly coupled interface.

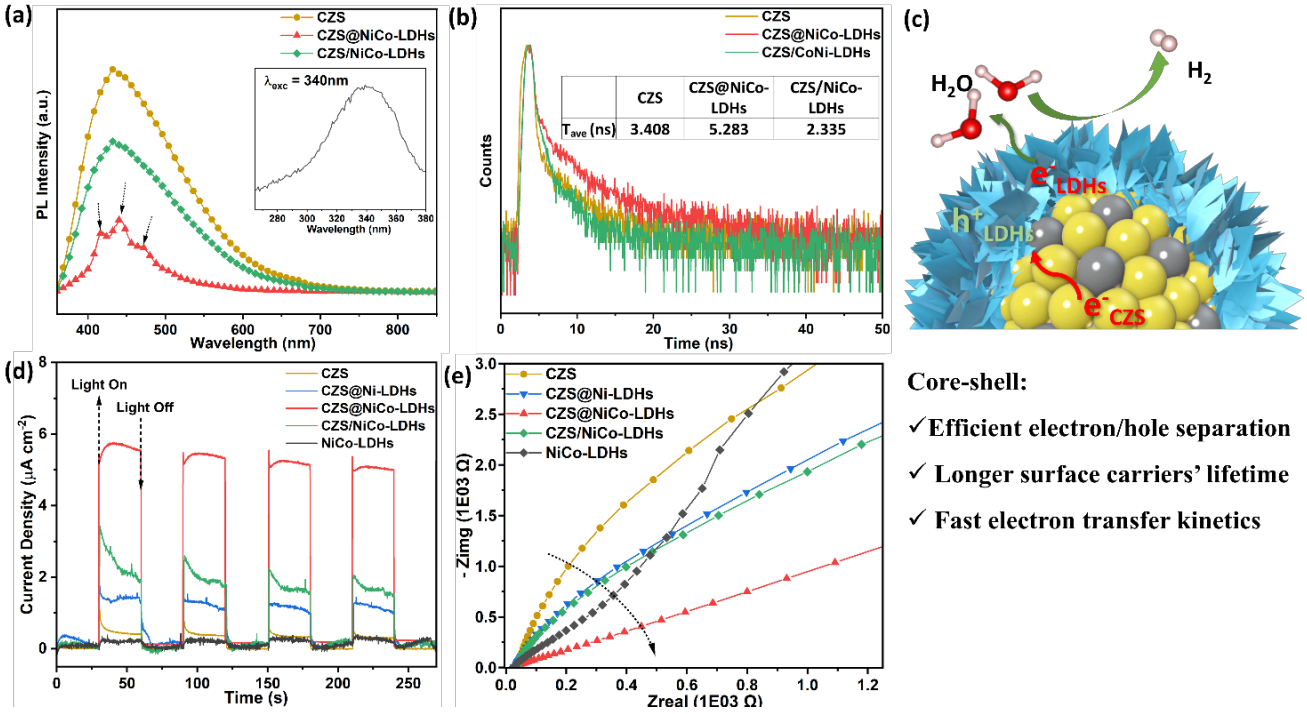

Figure 5. (a) Photoluminescence (PL) spectra (insert: excitation spectrum of CZS, λ_{exc} = 340 nm), (b) Time-resolved PL decay spectra (insert table: summary of electron lifetime) of CZS, CZS@NiCo-LDHs and CZS/NiCo-LDHs; (c) Illustration of advantages in the core-shell sample; (d) Chopped i-t curves under visible light irradiation (load 0.4 mg/cm^2), (e) Electrochemical impedance spectra (EIS) under illumination of CZS, CZS@Ni-LDHs, CZS@NiCo-LDHs, CZS/NiCo-LDHs in 0.1 M Na_2SO_4.

Transient photocurrent response plot at open circuit potential under visible irradiation was conducted to investigate the electron-hole separation capacity in samples (**Fig.5 d**). In this case, all prepared samples possess an anodic current, proving the n-type characteristics of samples. Due to the server electron-hole recombination, CZS itself exhibits a low photocurrent (0.38 μA cm^{-2}). Such low photocurrent is also observed in pure NiCo-LDHs sample (0.25 μA cm^{-2}), originating from the low visible-light absorption. After growing $Ni(OH)_2$ and NiCo-LDHs onto CZS surface, the corresponding photocurrent exhibits a significant increase to 1.14 μA cm^{-2} and 5.05 μA cm^{-2}, respectively. Such enhancement can be attributed to the fact that well-established interface

contributes to the transfer of excited electrons to the electrode instead of recombination with holes. Electrochemical impedance spectrum was also measured under illumination (**Fig.5 e**), proving the interfacial charge transfer ability. As indicated, CZS, as typical semiconductor, shows poorest electron transfer kinetics. After incorporating the LDHs into CZS system, it should be noticed all transfer kinetics are improved to certain extent, owing to the established interface, better electric conductivity. The CZS/NiCo-LDHs exhibited a significant larger semicircular arc than that of core-shell samples, indicating a larger charge transfer resistance. The CZS@NiCo-LDHs, as a result, possesses a better electrical conductivity, proving improved electron transfer resistance. This enhancement may be attributed to the abundant metal vacancies (V_{Zn}), which further promote the catalytic performance[40,43]. In a brief summary (**Fig.5 c**), the CZS@NiCo-LDHs exhibits an efficient electron-charge separation capacity, long lifetime of carries at LDHs surfaces, and improved electron transfer resistance.

2.5 Photocatalytic Mechanism Study

For in-depth analysis on the photocatalytic hydrogen evolution ability of each sample, the UV-vis DRS spectra and corresponding Tauc plots by adopting Kubelka–Munk function were recorded. As shown in **Fig.6 a** CZS possesses a typical light-yellow color, while pure NiCo-LDHs exhibit a brown color. After loading/mixing LDHs on/with CZS, such yellow color turns to green with different shades. Consistent with this color change phenomenon, the spectrum of CZS shows a typical absorption edge at 508 nm, lying under the visible light absorption region, which further suggests a band gap of 2.52 eV for CZS sample (**Fig.6 b**). However, the pure NiCo-LDHs, whose band gap is determined to be 2.43 eV, indicates an enhanced visible light absorption capability, with low capacity in UV region. Meanwhile, for both core-shell and composite samples, enhancement of absorption in the visible light region is observed. A further decrease in the absorption of UV light is observed in both core-shell and composite samples, which may be due to the shielding effect of LDHs. The band gaps of CZS@NiCo-LDHs and CZS/NiCo-LDHs are determined to be 2.45 eV and 2.55 eV, respectively. Based on above optical measurements, further Valence-band XPS (**Fig.S16**) were conducted to identify the potential heterojunction between CZS and NiCo-LDHs. The valence band potentials (VB_{xps}) of CZS and NiCo-LDHs are determined to be 2.37 eV and 1.45 eV. UPS measurements (**Fig.6 c**) were then recorded to determine the Fermi level (E_f) of corresponding CZS and NiCo-LDHs according to the equation (2)[44]:

$$E_f = V_{ac} - \phi \quad (2)$$

Where Vac is the vacuum level (assumed to be 0 eV). Hence, the E_f is determined to be -5.50 eV and -5.38 eV for CZS and NiCo-LDHs, respectively. The valence band maximum (VBM), as a result, can be determined to be -7.87 eV for CZS and -7.17 eV for NiCo-LDHs, accordingly (detailed

calculations can be found in supporting information). As indicated in **Fig.6 d**, the pristine CZS and NiCo-LDHs show an overlay in the band gap region, after exploring the corresponding E_{VB} and E_{CB} position. The conduction band edge and valence band edge of CZS and NiCo-LDHs will bend downward and upward accordingly when contacting with each other. Meanwhile, the electrons will transfer from NiCo-LDHs to CZS, due to the higher E_f level of LDHs, till the equilibrium. Such electron transfer pathway is inconsistent with above DFT simulations. Consequently, the contact potential difference can induce an electric field after the construction of interface[45]. This heterojunction further contributes to a direct Z-scheme heterojunction[46], where the excited electrons in the semiconductor will consume the holes remaining in the valence band of NiCo-LDHs under light irradiation. As a result, electrons at the conduction band of NiCo-LDHs will participate in the PHE reaction. Based on the above analysis, the primary reaction in the core-shell sample can be listed as follows:

$$CZS@NiCo-LDHs\ (s) + 2hv \rightarrow e^-_{CZS} + h^+_{CZS} + e^-_{NiCo-LDHs} + h^+_{NiCo-LDHs} \quad (3)$$

$$e^-_{CZS} + h^+_{NiCo-LDHs} \rightarrow recombnination \quad (4)$$

$$2\ e^-_{NiCo-LDHs} + 2H^+ \rightarrow H_2\ (g) \quad (5)$$

$$h^+_{CZS} + TEOA \rightarrow TEOA^+ \quad (6)$$

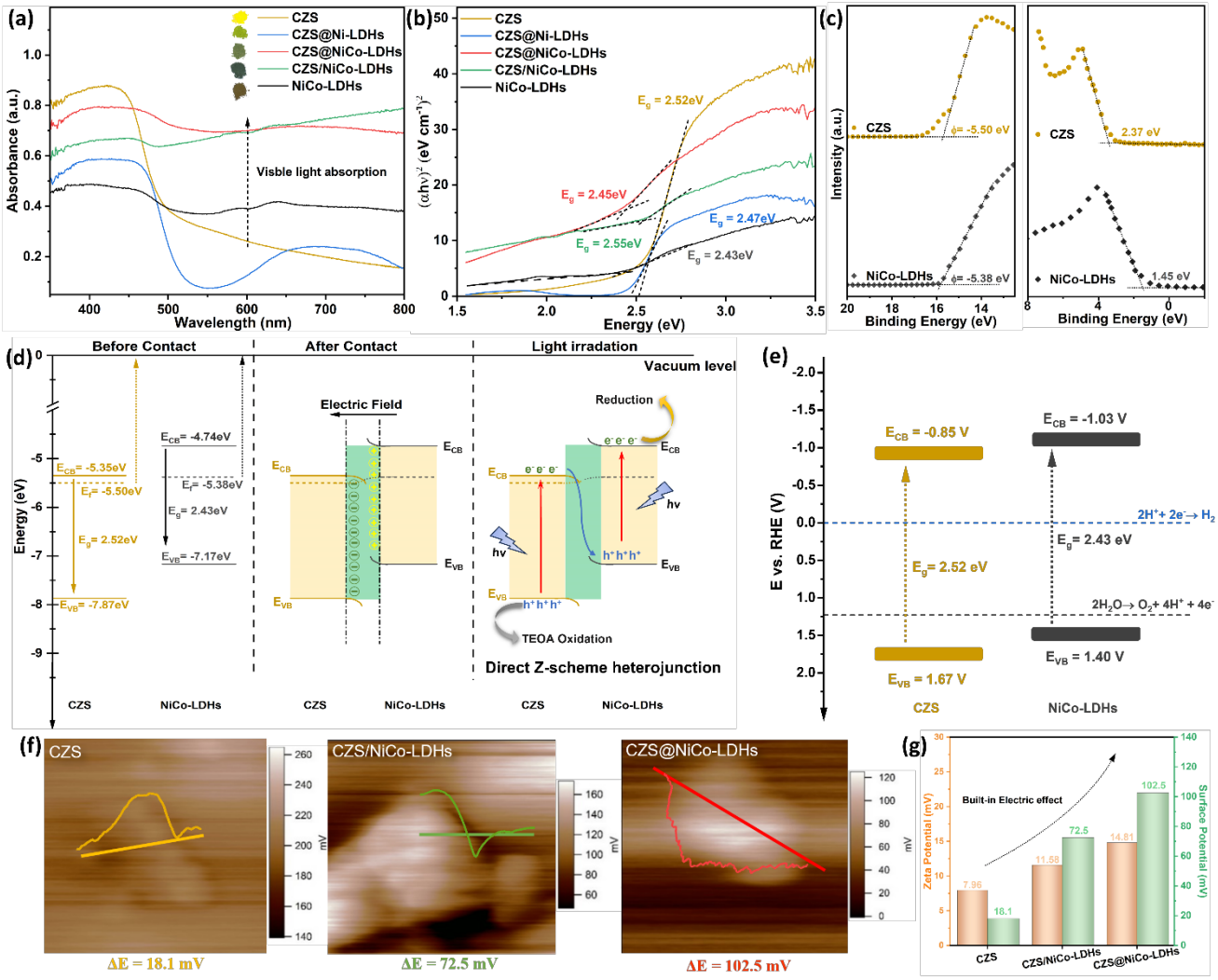

Figure 6. (a) UV-visible diffuse reflectance (UV-vis DRS) spectra, (b) Tauc plots of CZS, CZS@Ni-LDHs, CZS@NiCo-LDHs, CZS/NiCo-LDHs and NiCo-LDHs by assuming direct band configuration; (c) UPS (left) and valence band-XPS (right) spectra of CZS, NiCo-LDHs; (d) Band alignment between CZS and NiCo-LDHs under different conditions; (e) Band alignment of CZS, and NiCo-LDHs, derived from Mott-Schottky plot (V vs. reservable hydrogen evolution); (f) Kelvin-probe force microscopy of CZS, CZS/NiCo-LDHs, and CZS@NiCo-LDHs; and (g) Comparison between zeta potentials and surface potentials of CZS and CZS@NiCo-LDHs.

Moreover, Mott-Schottky measurement at fixed frequency was conducted to explore the samples' band alignment, which is related to the water splitting reaction potential (**Fig.S17**). The flat-band potential (E_{fb}) of CZS, CZS@NiCo-LDHs, and CZS/NiCo-LDHs composites were determined to be -0.85 V, -0.97 V and -0.92 V vs RHE, according to the intersection point at the potential axis ($1/C^2$ =0). The positive slope in the Mott-Schottky plot further suggests an "n-n" type semiconductor configuration in the prepared sample, again proving the existence of direct Z-scheme heterojunction in CZS@NiCo-LDHs. Usually, the E_{FB} of the n type semiconductors can be roughly equals to the

conduction potential[36,44]. By combining results from absorption spectrum (E_g = 2.52 eV for CZS and 2.43 eV for NiCo-LDHs), the band alignment of corresponding samples (**Fig.6 e**) exhibits a suitable region for both water reduction (0 V vs. RHE) and oxidation process (1.23 V vs. RHE). Atomic force microscopy with Kelvin probe, which is related to the surface charge density, was then employed to measure the surface potential of pristine CZS semiconductor and core-shell sample. The topological structure from the AFM image suggests the height of pristine CZS nanoparticles, CZS/NiCo-LDHs composites and CZS@NiCo-LDHs are 87.9 nm, 223.9 nm, and 135.5 nm, respectively (**Fig.S18**). Such topologies again prove the full coverage of LDHs onto the CZS semiconductor surface, with an approximate 20 nm in shell thickness. Voltage bias was subsequently applied to measure the surface potential of corresponding samples (**Fig.6 f,g**). Consequently, a positive surface potential is observed (102.5 mV) in the core shell sample, which is consistent with the Zeta potential results (7.96 mV to 14.81 mV). For the pure CZS, the KPFM value (18.1 mV) exhibits a slightly higher value than that of the Si background. This increasing shift confirms that the interface construction promotes a built-in electric field, which further promotes the catalytic performance.

3. Conclusion

To conclude, a surface modification treatment based on cadmium zinc sulfide system was proposed by taking advantage of small molecules with strong metal-affinity. The changes in surface micro-environment were identified by Zeta potential technique and further contributed to the full coverage of CZS by NiCo-layered double hydroxides. This heterostructure, which is further determined to be direct Z-scheme heterojunction, possesses an efficient charge-hole separation capability, longer surface carriers' lifetime, and faster electron transfer kinetics. Meanwhile, optical measurements and Mott-Schottky plot confirm a suitable alignment between CZS and NiCo-LDHs, where excited electrons of CZS will consume the holes left at valence band of NiCo-LDHs. As a result, a favorable visible-light driven PHE reaction (PHE rate= 18.75 mmol g^{-1} h^{-1}), good photo-stability (20 hrs) and a high AQE of 16.3% at 420 nm were achieved by this core-shell sample. Further DFT simulations and KPFM results confirm a built-in electric field CZS and NiCo-LDHs after the establishment of heterojunction. This innovation adopted from the nano architectonics and surface electronic environment modification, provides a new basis for further design of cocatalysts with distinguished heterojunctions.

4. Materials and Synthetic Procedures

Cadmium acetate dihydrate (98%), Zinc acetate dihydrate (98%), Cobalt acetate dihydrate (98%-102%), Nickel chloride tetrahydrate were purchased from Alfa Aesar (United States); Thiourea (99%+), Ammonia persulfate (98%+), Thioglycolic acid (TGA, 98%), Ammonia hydroxide (28 -30

wt%), Eosin Y (water soluble, 99%) were purchased from ACROS organics (UK); Potassium hydroxides pellets (99%+, ACS grade), Sodium sulfide (99%, ACS grade) were purchased from Aladdin (China). PVP (Mw = 58,000, K30), Ethylene glycol (99%+) were purchased from MACKLIN; Cd standard (1 mg/mL), Zn standard (1 mg/mL), Ni standard (1 mg/mL), Co standard (1 mg/mL) in 1% HNO_3 solution were purchased from Aladdin. Triethanolamine (99%) was obtained from Shanghai Chemical Reagent Co., Ltd. All chemicals were purchased and used without further purification.

4.1 Synthesis of $Cd_{0.75}Zn_{0.25}S$ and Surface Modification of CZS Nanospheres

To obtain CdZnS nanospheres, cadmium acetate dihydrate (0.84 g), zinc acetate dihydrate (0.19 g; Cd: Zn= 0.75:0.25 in molar ratio), and PVP (2 g, Mw = 54,000) were dissolved in 40 mL EG to form a clear solution A. Thiourea (0.80 g) as sulfur precursor was dissolved in 20 mL ethylene glycol to form solution B. The solution B was then drop added into pre-hot solution A to initiate the nucleation. The whole reaction takes place at 150℃ for 8 hrs. The samples were then precipitated by adding acetone and collected under centrifugation at 13,000 rpm for 10 min. The final products were obtained by vacuum drying at 60℃ overnight.

To modify the surface of CZS nanospheres, 100 μL of N_2 saturated thioglycolic acid (pH of acid is further tuned to 10) was added in to 10 mL of 20 mg/mL of CZS aqueous dispersion. The modification accounts for 3 hrs under vigorous stirring. The TGA-modified CZS nanospheres was collected under centrifugation at 10,000 rpm and redispersed into 10 mL DI H_2O for further use.

4.2 Synthesis of CZS@Ni-LDHs and CZS@NiCo-LDHs Core-shell Structure

To obtain core-shell structure, nickel chloride tetrahydrate (1.02 g), cobalt chloride tetrahydrate (0.35 g, Ni^{2+}: Co^{2+} = 3:1 in molar mass), and ammonia persulfate (0.34 g) were dissolved in 30 mL DI H_2O to form a clear solution C. Subsequently, 1mL, 4.5 mL and 13.5 mL of solution C was poured into above 10 mL TGA-modified CZS dispersion under stirring for 1 hour to achieve an adsorption equilibrium of metal ions. For pure Ni-LDHs, 1.304 g of nickel chloride tetrahydrate instead of mixture of nickel and cobalt salts was employed.

Subsequently, 0.7 mL of ammonia solution (28-30 wt%) was quickly injected into the above adsorption steady state solution. The whole solution was further transferred into a 50 mL Teflon kettle, and underwent 120℃ hydrothermal reactions for 8 hrs. The final CZS@Ni-LDHs, and CZS@NiCo-LDHs powders were separated, washed by centrifuging at 10,000 rpm using ethanol and DI H_2O respectively, which are further dried at 60℃ in a vacuum oven.

4.3 Synthesis of CZS/NiCo-LDHs Composites

To obtain CZS/NiCo-LDHs composites, 7 mL of above solution C was directly added to 10 mL of CZS aqueous dispersion, while other procedures remain the same.

Supporting Information

Supplementary data associated with this article can be found in the attached file.

Author Information

Corresponding Authors

Bin Fei- (a) School of Fashion & Textiles, (b) Research Institute for Intelligent Wearable Systems, The Hong Kong Polytechnic University, Hung Hom, Hong Kong 999077, China.

Email: bin.fei@polyu.edu.hk

Conflict of Interests

The authors declare no conflict of interests or personal relationships that could have appeared to influence the work reported in this paper.

Acknowledgements

We acknowledge the funding supports from PolyU RCRE (1-BBCB) and RI-IWEAR (1-CD8E).

References

[1] D. M. Fabian, S. Hu, N. Singh, F. A. Houle, T. Hisatomi, K. Domen, F. E. Osterloh, S. Ardo, *Energy Environ. Sci.* **2015**, *8*, 2825.

[2] J. Liu, Y. Liu, N. Liu, Y. Han, X. Zhang, H. Huang, Y. Lifshitz, S. T. Lee, J. Zhong, Z. Kang, *Science (80-.).* **2015**, *347*, 970.

[3] S. I. Naya, T. Kume, R. Akashi, M. Fujishima, H. Tada, *J. Am. Chem. Soc.* **2018**, *140*, 1251.

[4] Q. Xu, L. Zhang, B. Cheng, J. Fan, J. Yu, *Chem* **2020**, *6*, 1543.

[5] X. Zheng, Y. Song, Y. Liu, J. Li, Y. Yang, D. Wu, W. Liu, Y. Shen, X. Tian, *Small* **2023**, DOI 10.1002/smll.202207623.

[6] C. Cheng, J. Zhang, B. Zhu, G. Liang, L. Zhang, J. Yu, *Angew. Chemie - Int. Ed.* **2022**, *202218688*, DOI 10.1002/anie.202218688.

[7] Y. Chen, S. Zhao, X. Wang, Q. Peng, R. Lin, Y. Wang, R. Shen, X. Cao, L. Zhang, G. Zhou, J. Li, A. Xia, Y. Li, *J. Am. Chem. Soc.* **2016**, *138*, 4286.

[8] D. Ma, J. W. Shi, L. Sun, Y. Sun, S. Mao, Z. Pu, C. He, Y. Zhang, D. He, H. Wang, Y. Cheng,

Chem. Eng. J. **2022**, *431*, 133446.

[9] K. Li, H. Pan, F. Wang, Z. Zhang, S. Min, *Appl. Catal. B Environ.* **2023**, *321*, 122028.

[10] W. Jian, X. Cheng, Y. Huang, Y. You, R. Zhou, T. Sun, J. Xu, *Chem. Eng. J.* **2017**, *328*, 474.

[11] Z. Chen, H. Gong, Q. Liu, M. Song, C. Huang, *ACS Sustain. Chem. Eng.* **2019**, *7*, 16720.

[12] B. X. Zhou, S. S. Ding, B. J. Zhang, L. Xu, R. S. Chen, L. Luo, W. Q. Huang, Z. Xie, A. Pan, G. F. Huang, *Appl. Catal. B Environ.* **2019**, *254*, 321.

[13] L. Lai, F. Xing, C. Cheng, C. Huang, *Adv. Mater. Interfaces* **2021**, *8*, 1.

[14] Y. Wang, Y. H. Liu, Y. Zhang, F. Wang, P. J. Kowalski, H. W. Rohrs, R. A. Loomis, M. L. Gross, W. E. Buhro, *Angew. Chemie - Int. Ed.* **2012**, *51*, 6154.

[15] D. R. Nevers, C. B. Williamson, T. Hanrath, R. D. Robinson, *Chem. Commun.* **2017**, *53*, 2866.

[16] M. Wang, Z. Wan, X. Meng, Z. Li, X. Ding, P. Li, C. Li, J. G. Wang, Z. Li, *Appl. Catal. B Environ.* **2022**, *309*, 121272.

[17] B. X. Zhou, S. S. Ding, K. X. Yang, J. Zhang, G. F. Huang, A. Pan, W. Hu, K. Li, W. Q. Huang, *Adv. Funct. Mater.* **2021**, *31*, 1.

[18] Q. Chi, G. Zhu, D. Jia, W. Ye, Y. Wang, J. Wang, T. Tao, F. Xu, G. Jia, W. Li, P. Gao, **2021**, 4496.

[19] D. W. Su, J. Ran, Z. W. Zhuang, C. Chen, S. Z. Qiao, Y. D. Li, G. X. Wang, *Sci. Adv.* **2020**, *6*, 1.

[20] P. Zhang, B. Y. Guan, L. Yu, X. W. (David) Lou, *Chem* **2018**, *4*, 162.

[21] B. Fang, Z. Xing, F. Du, W. Kong, Z. Li, W. Zhou, *J. Mater. Chem. A* **2022**, *10*, 16439.

[22] D. Huang, M. Wen, C. Zhou, Z. Li, M. Cheng, S. Chen, W. Xue, L. Lei, Y. Yang, W. Xiong, W. Wang, *Appl. Catal. B Environ.* **2020**, *267*, 118651.

[23] S. Li, L. Wang, Y. D. Li, L. Zhang, A. Wang, N. Xiao, Y. Gao, N. Li, W. Song, L. Ge, J. Liu, *Appl. Catal. B Environ.* **2019**, *254*, 145.

[24] X. Han, J. Li, J. Lu, S. Luo, J. Wan, B. Li, C. Hu, X. Cheng, *Nano Energy* **2021**, *86*, 106079.

[25] C. He, L. Yang, X. Peng, S. Liu, J. Wang, C. Dong, D. Du, **2023**, DOI 10.1021/acsnano.2c12735.

[26] L. Zeiri, I. Patla, S. Acharya, Y. Golan, S. Efrima, *J. Phys. Chem. C* **2007**, *111*, 11843.

[27] X. Bai, Z. Ren, S. Du, H. Meng, J. Wu, Y. Xue, X. Zhao, H. Fu, *Sci. Bull.* **2017**, *62*, 1510.

[28] M. Luo, Y. Liu, J. Hu, H. Liu, J. Li, *ACS Appl. Mater. Interfaces* **2012**, *4*, 1813.

[29] F. Song, X. Hu, *Nat. Commun.* **2014**, *5*, DOI 10.1038/ncomms5477.

[30] Z. Yan, Z. Sun, X. Liu, H. Jia, P. Du, *Nanoscale* **2016**, *8*, 4748.

[31] L. Zhang, X. Fu, S. Meng, X. Jiang, J. Wang, S. Chen, *J. Mater. Chem. A* **2015**, *3*, 23732.

[32] H. Xue, A. Meng, H. Zhang, Y. Lin, Z. Li, C. Wang, *Nano Res.* **2021**, *12*, DOI 10.1007/s12274-021-3359-2.

[33] Z. Li, Y. Zhou, M. Xie, H. Cheng, T. Wang, J. Chen, Y. Lu, Z. Tian, Y. Lai, G. Yu, *Angew. Chemie - Int. Ed.* **2023**, *78712*, DOI 10.1002/anie.202217815.

[34] F. Gao, R. Lei, X. Huang, J. Yuan, C. Jiang, W. Feng, L. Zhang, P. Liu, *Appl. Catal. B Environ.* **2021**, *292*, 120187.

[35] S. Liu, W. Qi, J. Liu, X. Meng, S. Adimi, J. P. Attfield, M. Yang, *ACS Catal.* **2023**, 2214.

[36] M. Wang, J. Q. Wang, C. Xi, C. Q. Cheng, C. Q. Zou, R. Zhang, Y. M. Xie, Z. L. Guo, C. C. Tang, C. K. Dong, Y. J. Chen, X. W. Du, *Angew. Chemie - Int. Ed.* **2020**, *59*, 11510.

[37] Y. Jiao, Y. Zheng, M. Jaroniec, S. Z. Qiao, *Chem. Soc. Rev.* **2015**, *44*, 2060.

[38] M. Huang, C. Liu, P. Cui, T. Wu, X. Feng, H. Huang, J. Zhou, Y. Wang, *Environ. Sci. Technol.* **2021**, *55*, 13132.

[39] Y. H. Hsieh, C. P. Huang, *Colloids and Surfaces* **1991**, *53*, 275.

[40] B. Xiao, T. Lv, J. Zhao, Q. Rong, H. Zhang, H. Wei, J. He, J. Zhang, Y. Zhang, Y. Peng, Q. Liu, *ACS Catal.* **2021**, *11*, 13255.

[41] H. Tang, G. Xu, L. Weng, L. Pan, L. Wang, *Acta Mater.* **2004**, *52*, 1489.

[42] Q. Zhu, B. Qiu, H. Duan, Y. Gong, Z. Qin, B. Shen, M. Xing, J. Zhang, *Appl. Catal. B Environ.* **2019**, *259*, 118078.

[43] Y. Lin, Q. Zhang, Y. Li, Y. Liu, K. Xu, J. Huang, X. Zhou, F. Peng, *ACS Sustain. Chem. Eng.* **2020**, *8*, 4537.

[44] L. Wang, B. Cheng, L. Zhang, J. Yu, *Small* **2021**, *17*, 2103447.

[45] L. Zhai, X. She, L. Zhuang, Y. Li, R. Ding, X. Guo, Y. Zhang, Y. Zhu, K. Xu, H. J. Fan, S. P. Lau, *Angew. Chemie* **2022**, *134*, 1.

[46] B. X. Zhou, S. S. Ding, Y. Wang, X. R. Wang, W. Q. Huang, K. Li, G. F. Huang, *Nanoscale* **2020**, *12*, 6037.